

NONLINEAR STRUCTURAL ANALYSIS BY MINIMIZING TWO KINDS OF ENERGIES

M. Rezaiee-Pajand^{1,*},[†] and H. Estiri²

1. Department of Civil Engineering, Ferdowsi University of Mashhad, Mashhad, Iran

2. Department of Civil Engineering, University of Gonabad, Gonabad, Iran

ABSTRACT

One of the goals of the nonlinear structural analysis is to reduce the required time for obtaining the numerical solution. More important than this issue, the nonlinear scheme could converge to the answers for all types of problems. A perfect nonlinear solver must have both of these specifications. This article aims to reduce the duration of structural analysis as well as to boost convergent requirements. To reach these two objectives, the authors simultaneously minimize the kinetic and residual structural energies. The ability of the new formulation is shown by solving several structures, with nonlinear geometrical behavior. Based on the compressive studies, numerical solutions show the high efficiency of the new method.

Keywords: Kinetic energy, Residual energy, Dynamic relaxation, Equilibrium path, Load factor, Limit points.

Received: 12 December 2024; Accepted: 28 January 2025

1. INTRODUCTION

The common dynamic relaxation algorithm (DR) cannot easily trace the structural static path. In this technique, the jumps occur at the limit points. To fix this defect, a variable load factor is formulated. In the structural static analysis, the following general equation should be solved:

$$\mathbf{SX} = \mathbf{P} \quad (1)$$

Here, the stiffness matrix is shown by S . Moreover, X and P , are the displacement and load vectors, respectively. In the nonlinear structural analysis, the stiffness matrix and the

*Corresponding author: Department of Civil Engineering, Ferdowsi University of Mashhad, Mashhad, Iran

[†]E-mail address: rezaiee@um.ac.ir (M. Rezaiee-Pajand)

internal forces are nonlinear functions of the nodal displacements. Hence, the iterative procedures are used to solve the system. So far, a lot of researchers have proposed various relationships for nonlinear structural analysis. One way of solving Eq. (1) is utilizing the dynamic relaxation (DR) scheme. In this process, artificial mass and damping are added to Eq. (1). As a result, the next equation is obtained:

$$\mathbf{M}\ddot{\mathbf{X}} + \mathbf{C}\dot{\mathbf{X}} + \mathbf{S}\mathbf{X} = \mathbf{P} \quad (2)$$

Where, the fictitious damping and mass matrices are denoted by \mathbf{C} and \mathbf{M} , correspondingly. Moreover, $\ddot{\mathbf{X}}$ and $\dot{\mathbf{X}}$ are the acceleration and velocity vectors, respectively. It should be noted that the DR approach is considered to be an explicit technique. Because the mass and damping matrices are assumed to be diagonal. The DR method has two types of viscous and kinetic formulations. Especially, the kinetic dynamic relaxation approach applies to form-finding cable and membrane structures [1]. Alamatian proposed a new relation for estimating fictitious mass [2]. Namadchi and Alamatian used the DR for dynamic analysis of structures [3]. Jung et al. calculated the time step based on continuous kinetic damping [4]. Rezaiee-Pajand and Mohammadi-Khatami obtained a formula for the fictitious time step for the viscous dynamic relaxation [5].

The efficiency of dynamic relaxation methods in static analysis of 3D cable structures was examined by Hüttner et al. [6]. In a comprehensive comparison study, the abilities of 51 different dynamic relaxation procedures were found, and the obtained results were presented [7]. Another application of DR scheme is related to tracing the structural equilibrium path. By applying this method, a nonlinear buckling load and the limit points could be obtained. These goals can be accomplished by using a variable load factor. The kinetic DR method has been used for the form-finding of structures [8]. Form-finding and analysis of tension structures by dynamic relaxation were evaluated by Barnes [9]. Moncrieff and Topping introduced a new procedure for generating cutting patterns for membrane structures, employing a two-dimensional dynamic relaxation analysis for each cloth [10]. In another research, a parallel algorithm for the DR strategy was presented by Topping and Khan [11].

In the following part, the previous investigations on the tracing of the structural equilibrium path are reviewed in the last decade. Lee et al. proposed a formula for the post-buckling path of structures, by combining the explicit arc length approach and the kinetic DR [12]. Rezaiee-Pajand and Alamatian obtained two formulas to trace the equilibrium path. They were based on minimizing the unbalanced energy and residual force [13]. Alamatian suggested two other relations by minimizing the kinetic energy and the unbalanced displacement [14]. Lee et al. used two implicit and explicit arc length processes to analyze the post-buckling of space frames [15]. Rezaiee-Pajand and Estiri also established four formulas to estimate the load factor for finding the structural static path [16, 17, 18, 19]. The nonlinear thermo-elastic bending analysis of a functionally graded carbon nanotube-reinforced composite plate resting on two-parameter elastic foundations was investigated by Golmakani and Zeighami [20]. In another study, Golmakani and Kadkhodayan investigated the axisymmetric bending and stretching of circular and annular functionally graded plates with variable thickness under combined thermal-mechanical loading and various boundary conditions [21]. A new parallelization approach was programmed with the NVIDIA CUDA

API proposed by Iványi [22]. The adaptive dynamic relaxation approach is used to solve linear elastic and crack propagation problems [23].

In this research, a new equation is proposed for the load factor by minimizing kinetic and residual energy, simultaneously. For this purpose, the sum of the kinetic and residual energy is assumed to be based on the DR artificial parameters. Then, this relation is minimized and a new formula is achieved for the load factor. As a result, the proposed load factor depends only on the fictitious parameters used in the DR process. To show the significance of the authors' formulation, the ability of the suggested approach is evaluated by performing several numerical examples. Furthermore, the recommended formula is compared with other researchers' solutions, based on the number of iterations, and the number of converging points on the static path of the analysis time. The authors in this paper aim to find a formula that obtains the convergence points in the statical path in a shorter time. In other words, the time to reach each convergence point should be reduced. Furthermore, reducing the time of each iteration is another advantage of the proposed method.

2. THE DYNAMIC RELAXATION PROCESS

By using the central finite difference relations for Eq. (2), the fundamental relations of dynamic relaxation are obtained. Equations (3) and (4) show the velocity and displacement in the dynamic relaxation approach, respectively [1].

$$\dot{\mathbf{X}}_i^{n+\frac{1}{2}} = \frac{2\mathbf{M}_{ii}^n - \mathbf{C}_{ii}^n t^n}{2\mathbf{M}_{ii}^n + \mathbf{C}_{ii}^n t^n} \dot{\mathbf{X}}_i^{n-\frac{1}{2}} + \frac{2t^n}{2\mathbf{M}_{ii}^n + \mathbf{C}_{ii}^n t^n} (\mathbf{P}_i^n - \mathbf{F}_i^n) \quad , \quad i=1,2,\dots,ndof \quad (3)$$

$$\mathbf{X}_i^{n+1} = \mathbf{X}_i^n + t^{n+\frac{1}{2}} \dot{\mathbf{X}}_i^{n+\frac{1}{2}} \quad , \quad i=1,2,\dots,ndof \quad (4)$$

The artificial time step, i -th entry of the internal force, and the external force vectors in the repetition of the n -th, are shown by t^n , \mathbf{F}_i^n and \mathbf{P}_i^n , correspondingly. The number of degrees of freedom is displayed with $ndof$.

In the process of accomplishing the responses, both equations (3) and (4) are repeated until the residual force reaches an acceptable error. In DR method, the unbalanced force causes the artificial oscillation of the structure. The unbalanced force vector of \mathbf{R} is obtained from the difference between internal and external forces, as follows:

$$\mathbf{R} = \mathbf{P} - \mathbf{F} \quad (5)$$

Parameters influencing the dynamic relaxation procedure are mass and damping matrices. Researchers have proposed a variety of methods for estimating these factors. Underwood used equality (6) for the mass matrix [24]. He considered the time step value to be equal to 1.1.

$$\mathbf{M}_{ii} = \frac{t^2}{4} \sum_{j=1}^{ndof} |\mathbf{S}_{ij}| \quad (6)$$

Zhang and Yu obtained a relationship for fictitious damping. They suggested this factor from Rayleigh's principle, in the following form [25].

$$\omega_0 = \frac{\mathbf{X}^T \mathbf{F}}{\mathbf{X}^T \mathbf{M} \mathbf{X}} \quad (7)$$

$$\mathbf{C} = 2\omega_0 \mathbf{M} \quad (8)$$

In another study and by minimizing the displacement error of two consecutive iterations, Rezaei-Pajand and Alamatian recommended equations (9) and (10) for artificial mass and damping, respectively [26]. These researchers estimated the minimum factious frequency from Eq. (7).

$$\mathbf{M}_{ii} = \max \left(\frac{t^2}{2} \mathbf{S}_{ii}, \frac{t^2}{4} \sum_{j=1}^{ndof} |\mathbf{S}_{ij}| \right) \quad (9)$$

$$\mathbf{C} = \sqrt{\omega_0^2 (4 - t^2 \omega_0^2)} \mathbf{M} \quad (10)$$

In the common dynamic relaxation formulation, the external load is constant in each load step. Because of this assumption, jumps usually occur near the snap-back and snap-through regions. Hence, the conventional dynamic relaxation procedures cannot always cross the limit points. Figure 1 shows jumping on the structural static path at the force limit point. If the usual dynamic relaxation is used, at point A, the response moves to point B with a slight increase in the load amount. To pass through the return parts in the dynamic relaxation algorithm, the variable external load must be applied. For this reason, Eq. (11) is used instead of Eq. (5) to calculate the residual force. The symbol λ is the load factor. By utilizing this parameter, the load level will be variable.

$$\mathbf{R} = \lambda \mathbf{P} - \mathbf{F} \quad (11)$$

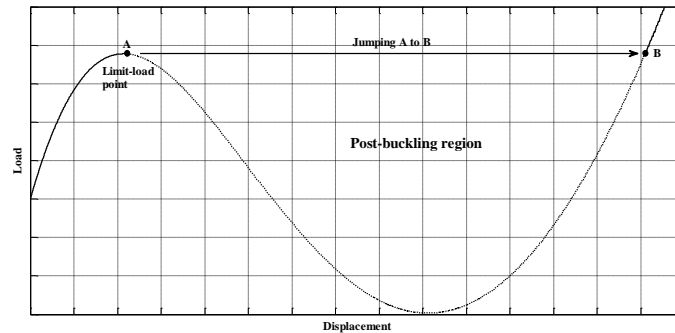


Figure 1: The conventional DR technique at the limit points

Rezaei-Pajand and Alamatian minimized the unbalanced force and the residual energy. Accordingly, they obtained the two relations (12) and (13) for the load factor in each dynamic relaxation iteration, respectively [13].

$$\lambda = \frac{\mathbf{P}^T \mathbf{F}}{\mathbf{P}^T \mathbf{P}} \tag{12}$$

$$\lambda = \frac{\sum_{i=1}^{ndof} \frac{\mathbf{P}_i}{2\mathbf{M}_{ii}^n + \mathbf{C}_{ii}^n t^n} \left[4t^n \mathbf{F}_i^n - (2\mathbf{M}_{ii}^n - \mathbf{C}_{ii}^n t^n) \dot{\mathbf{X}}_i^{n-\frac{1}{2}} \right]}{4t^n \sum_{i=1}^{ndof} \frac{(\mathbf{P}_i)^2}{2\mathbf{M}_{ii}^n + \mathbf{C}_{ii}^n t^n}} \tag{13}$$

In addition, Alamatian suggested equations (14) and (15), based on minimizing the unbalanced displacement and the residual kinetic energy, respectively [14].

$$\lambda = \frac{\sum_{i=1}^{ndof} \frac{\mathbf{P}_i}{(2\mathbf{M}_{ii}^n + \mathbf{C}_{ii}^n t^n)^2} \left[2t^n \mathbf{F}_i^n - (2\mathbf{M}_{ii}^n - \mathbf{C}_{ii}^n t^n) \dot{\mathbf{X}}_i^{n-\frac{1}{2}} \right]}{2t^n \sum_{i=1}^{ndof} \left(\frac{\mathbf{P}_i}{2\mathbf{M}_{ii}^n + \mathbf{C}_{ii}^n t^n} \right)^2} \tag{14}$$

$$\lambda = \frac{\sum_{i=1}^{ndof} \mathbf{P}_i \left(\frac{\mathbf{M}_{ii}^n}{2\mathbf{M}_{ii}^n + \mathbf{C}_{ii}^n t^n} \right)^2 \left[2t^n \mathbf{F}_i^n - (2\mathbf{M}_{ii}^n - \mathbf{C}_{ii}^n t^n) \dot{\mathbf{X}}_i^{n-\frac{1}{2}} \right]}{2t^n \sum_{i=1}^{ndof} \left(\frac{\mathbf{M}_{ii}^n \mathbf{P}_i}{2\mathbf{M}_{ii}^n + \mathbf{C}_{ii}^n t^n} \right)^2} \tag{15}$$

In another study, Rezaei-Pajand and Estiri obtained some relationships for the load coefficient [16, 17, 18, 19]. In one of them, they minimized external work with respect to the load factor. Eq. (16) shows the load factor in the mentioned method. This increment is added to the previous load coefficient to estimate the load factor in the new step [18].

$$\delta\lambda^n = \frac{-\sum_{i=1}^{ndof} \frac{\mathbf{P}_i}{2\mathbf{M}_{ii}^n + \mathbf{C}_{ii}^n t^n} \left[2t^n \mathbf{R}_i^{n-1} + (2\mathbf{M}_{ii}^n - \mathbf{C}_{ii}^n t^n) \dot{\mathbf{X}}_i^{n-\frac{1}{2}} \right]}{\sum_{i=1}^{ndof} \frac{4t^n}{2\mathbf{M}_{ii}^n + \mathbf{C}_{ii}^n t^n} (\mathbf{P}_i)^2} \tag{16}$$

In another relation, they suggested a new way to find the load factor increment by setting the work increment of external forces. Eq. (17) shows their proposed factor [16].

$$\delta\lambda^n = \frac{-\sum_{i=1}^{ndof} \frac{\mathbf{P}_i}{2\mathbf{M}_{ii}^n + \mathbf{C}_{ii}^n t^n} \left[2t^n \mathbf{R}_i^{n-1} + (2\mathbf{M}_{ii}^n - \mathbf{C}_{ii}^n t^n) \dot{\mathbf{X}}_i^{n-\frac{1}{2}} \right]}{\sum_{i=1}^{ndof} \frac{2t^n}{2\mathbf{M}_{ii}^n + \mathbf{C}_{ii}^n t^n} (\mathbf{P}_i)^2} \quad (17)$$

3. PROPOSED METHOD

In this study, a new formula is obtained for the load factor by minimizing the sum of the kinetic energy and the residual energy with respect to this coefficient. Based on the artificial factors of the dynamic relaxation technique, the kinetic energy and residual energy are estimated from Eqs. (18) and (19), respectively.

$$KE = \frac{1}{2} \mathbf{M} \dot{\mathbf{X}}^2 = \sum_{i=1}^{ndof} \frac{1}{2} \mathbf{M}_{ii}^n \left(\dot{\mathbf{X}}_i^{n+\frac{1}{2}} \right)^2 = \sum_{i=1}^{ndof} \frac{1}{2} \mathbf{M}_{ii}^n \left(\frac{2\mathbf{M}_{ii}^n - \mathbf{C}_{ii}^n t^n}{2\mathbf{M}_{ii}^n + \mathbf{C}_{ii}^n t^n} \dot{\mathbf{X}}_i^{n-\frac{1}{2}} + \frac{2t^n}{2\mathbf{M}_{ii}^n + \mathbf{C}_{ii}^n t^n} \mathbf{R}_i^n \right)^2 \quad (18)$$

$$RE = \mathbf{R} \delta \mathbf{X} = \sum_{i=1}^{ndof} \mathbf{R}_i^n \delta \mathbf{X}_i^n = \sum_{i=1}^{ndof} \mathbf{R}_i^n t^n \left(\frac{2\mathbf{M}_{ii}^n - \mathbf{C}_{ii}^n t^n}{2\mathbf{M}_{ii}^n + \mathbf{C}_{ii}^n t^n} \dot{\mathbf{X}}_i^{n-\frac{1}{2}} + \frac{2t^n}{2\mathbf{M}_{ii}^n + \mathbf{C}_{ii}^n t^n} \mathbf{R}_i^n \right) \quad (19)$$

Then, the amount of residual force of Eq. (11) is inserted in the above equations. Next, these two functions are summed. After simplifying and defining the following factors, A_n and B_n , equation (21) is obtained.

$$A^n = \frac{2\mathbf{M}_{ii}^n - \mathbf{C}_{ii}^n t^n}{2\mathbf{M}_{ii}^n + \mathbf{C}_{ii}^n t^n} \dot{\mathbf{X}}_i^{n-\frac{1}{2}} \quad (20)$$

$$B^n = \frac{2t^n}{2\mathbf{M}_{ii}^n + \mathbf{C}_{ii}^n t^n}$$

$$KE + RE = \frac{1}{2} \mathbf{M}_{ii}^n \left[(\lambda^n \mathbf{B}^n \mathbf{P}_i^n)^2 + 2\lambda^n A^n \mathbf{B}^n \mathbf{P}_i^n - 2\lambda^n (B^n)^2 \mathbf{P}_i^n \mathbf{F}_i^n - 2A^n \mathbf{B}^n \mathbf{F}_i^n + (B^n \mathbf{F}_i^n)^2 + (A^n)^2 \right] + \left[(\lambda^n \mathbf{P}_i^n)^2 \mathbf{B}^n t^n + \lambda^n A^n \mathbf{P}_i^n t^n - 2\lambda^n \mathbf{B}^n \mathbf{P}_i^n \mathbf{F}_i^n t^n - A^n \mathbf{F}_i^n t^n + B^n (\mathbf{F}_i^n)^2 t^n \right] \quad (21)$$

Now, the load factor λ must be calculated in such a way that Eq. (23) is minimized. The necessary condition for minimizing this function is that the first derivative with respect to load factor is equal to zero. The derivative of Eq. (21) is obtained in Eq. (22).

$$\lambda^n \left[(\mathbf{B}^n \mathbf{P}_i^n)^2 \mathbf{M}_{ii}^n + 2\mathbf{B}^n (\mathbf{P}_i^n)^2 t^n \right] + \left[A^n \mathbf{B}^n \mathbf{P}_i^n \mathbf{M}_{ii}^n - (B^n)^2 \mathbf{P}_i^n \mathbf{F}_i^n \mathbf{M}_{ii}^n + A^n \mathbf{P}_i^n t^n - 2\mathbf{B}^n \mathbf{P}_i^n \mathbf{F}_i^n t^n \right] = 0$$

$$\lambda^n = \frac{-\left[A^n \mathbf{B}^n \mathbf{P}_i^n \mathbf{M}_{ii}^n - (B^n)^2 \mathbf{P}_i^n \mathbf{F}_i^n \mathbf{M}_{ii}^n + A^n \mathbf{P}_i^n t^n - 2\mathbf{B}^n \mathbf{P}_i^n \mathbf{F}_i^n t^n \right]}{(\mathbf{B}^n \mathbf{P}_i^n)^2 \mathbf{M}_{ii}^n + 2\mathbf{B}^n (\mathbf{P}_i^n)^2 t^n} \quad (22)$$

In addition, a sufficient condition for minimization Eq. (21) is that its second derivative is positive for the load factor. Eq. (23) shows that the second derivative is always positive. Hence, the load factor (22) minimizes the function (21).

$$\frac{d^2(KE + RE)}{d(\lambda^n)^2} = \left[(B^n \mathbf{P}_i^n)^2 m_{ii}^n + 2B^n (\mathbf{P}_i^n)^2 t^n \right] > 0 \tag{23}$$

Finally, by inserting the factors of A_n and B_n into Eq. (22), the load factor of Eq. (24) can be found.

$$\lambda^n = \frac{\sum_{i=1}^{ndof} \mathbf{P}_i \left\{ \frac{2\mathbf{M}_{ii}^n}{2\mathbf{M}_{ii}^n + t^n \mathbf{C}_{ii}^n} \left[2t^n \mathbf{F}_i^n - (2\mathbf{M}_{ii}^n - t^n \mathbf{C}_{ii}^n) \dot{\mathbf{X}}_i^{n-\frac{1}{2}} \right] + \left[4t^n \mathbf{F}_i^n - (2\mathbf{M}_{ii}^n - t^n \mathbf{C}_{ii}^n) \dot{\mathbf{X}}_i^{n-\frac{1}{2}} \right] \right\}}{\sum_{i=1}^{ndof} \frac{4t^n (\mathbf{P}_i)^2}{2\mathbf{M}_{ii}^n + t^n \mathbf{C}_{ii}^n} \left[\frac{\mathbf{M}_{ii}^n}{2\mathbf{M}_{ii}^n + t^n \mathbf{C}_{ii}^n} + 1 \right]} \tag{24}$$

It is worth emphasizing that the new proposed formula depends only on the DR parameters. The dynamic relaxation steps to trace the static path are as follows:

- Step 1- Assume the first values of velocity and displacement are zero.
- Step 2- The internal force vector and the stiffness matrix are established. This matrix is only for estimating the artificial mass and there is no need for matrix calculations in the solution process.
- Step 3- Form the artificial damping and mass matrices.
- Step 4- Obtain the load factor from equations (12) to (17) or (24), based on the desired technique.
- Step 5- Calculate the force vector of Eq. (11).
- Step 6- if $\left\| \frac{\mathbf{R}^T \mathbf{R}}{\mathbf{P}^T \mathbf{P}} \right\| < e_R$, go to Step 8. Otherwise, update velocities from Eq. (3).
- Step 7- Update the nodal displacements by Eq. (4). Go to Step 2.
- Step 8- Print the load factor and the displacements of the current increment.
- Step 9- If the target displacements or the target loads are achieved, the analysis procedure finishes. Otherwise, assume $\lambda = \lambda + 1$, and return to Step 2.

4. NUMERICAL EXAMPLES

Using a Fortran code, the required computer program is written for applying all the seven procedures of the previous sections. By utilizing this program, various structures with nonlinear geometric behavior are analyzed in this study. The load-displacement curve of many of these examples has been obtained by previous researchers and they are used to check the accuracy of the proposed method. For each sample, the structural static path is plotted. The mass matrix is obtained from the Underwood method. The time step is assumed equal to one. Moreover, the Zhang process is utilized to estimate the damping factor. To

compare the performances of all techniques, the analysis duration time and the number of iterations of each structure are listed in the tables. The following three criteria are used to compare the solutions:

$$S1 = \frac{\text{Total Number of Iterations}}{\text{Number of Converged Points}}, \quad S2 = \frac{\text{Total Iterations}}{\text{IterationTimes}}, \quad S3 = \frac{\text{IterationTimes}}{\text{Number of Converged Points}} \quad (25)$$

The symbol S1 represents the number of effective iterations to reach a convergence point. The smaller S1 shows that the convergence points are obtained with fewer iterations. In other words, a smaller value of S1 indicates the superiority of that method. Furthermore, factor S2 indicates the number of repetitions per second of the analysis time. Contrary to the previous criterion, a higher value of S2 indicates the superiority of the method. In other words, the more the value of S2, the higher the number of repetitions in less time. The S3 criterion is the time required to reach a converged point. Here, a lower value for S3 indicates a shorter analysis time per convergence point. The small number of convergence points reduces the analysis time. On the other hand, more convergence points are needed to find a more accurate structural static path. As a result, the analysis time increases. Table 1 shows the processes and symbols of the solutions used in this paper. It is found that some methods take a shorter time to reach the answer, but the number of convergence points is fewer. As a result, these approaches are not accurate. For this reason, both the number of convergence points and the analysis time should be considered. In other words, the shorter analysis time does not necessarily mean that the procedure is good.

Table 1: The used DR strategies and their indications

| Method | Symbol | Method base | Equation |
|----------|--------|---|----------|
| Previous | MRF | Minimization of Residual Force | (12) |
| | MRE | Minimization of Residual Energy | (13) |
| | MDI | Minimization of Displacement Increment | (14) |
| | MKE | Minimization of Kinetic Energy | (15) |
| | MEW | Minimization of External forces Work increment in repetitions | (16) |
| | ZWI | Zero the external forces Work Increment in repetitions | (17) |
| Proposed | MRaKE | Minimization of Residual Energy and Kinetic Energy | (24) |

4.1. Two members' truss

To verify suggested formulations and the authors' computer code, the two-member truss in Figure 2 is analyzed. Greco et al. investigated this simple supported truss. The module of elasticity and cross-section of each member are 71.7 GPa and 60 mm², respectively [27]. This truss has a degree of freedom. Because its geometry and loading are symmetrical. This degree is the vertical displacement of the middle node.

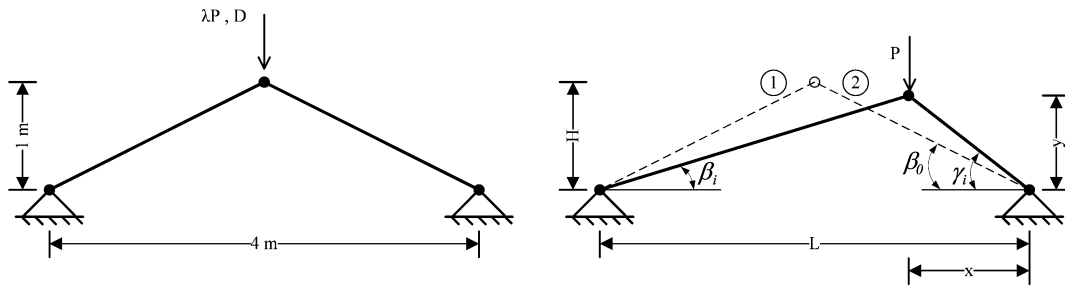


Figure 2: Two-member truss

It should be noted that the closed-form solution of this truss has been obtained by researchers [28]. Equations (26) and (27) show the static equilibrium of this structure. Young’s module and the cross-section of the members are shown by E and A , correspondingly. Subscripts 1 and 2 refer to the member number.

$$-\frac{\cos \gamma_i}{\cos \beta_i} \frac{P}{\cos \gamma_i \cdot \tan \beta_i + \sin \gamma_i} = E_1 A_1 \left[2 \frac{L-x \cos \beta_0}{L \cos \beta_i} - 1 \right] \tag{26}$$

$$-\frac{P}{\cos \gamma_i \cdot \tan \beta_i + \sin \gamma_i} = E_2 A_2 \left[2 \frac{x \cos \beta_0}{L \cos \gamma_i} - 1 \right] \tag{27}$$

By solving two Eqs (26) and (27), Felippa estimated the tangential stiffness matrix \mathbf{K} and the middle node displacement D_y [29]. These values are represented by Eqs (28) and (29), respectively.

$$\mathbf{K} = \frac{8EA}{\sqrt{(4H^2+L^2)^3}} \left[3D_y^2 + 6HD_y + 2H^2 \right] \tag{28}$$

$$\lambda \mathbf{P} = \frac{4EA}{\sqrt{(4H^2+L^2)^3}} \left[2(H+D_y)(2HD_y+D_y^2) \right] \tag{29}$$

At the load limit point, the stiffness matrix determinant is zero. If Eq. (28) is equal to zero, the displacement is obtained at this point. Equation (30) indicates this value.

$$3D_y^2 + 6HD_y + 2H^2 = 0 \quad \rightarrow \quad D_y = -H \pm \frac{H}{\sqrt{3}} \tag{30}$$

By replacing the value of H in Eq. (30), two numbers are calculated from the displacement expression. Then, if these values substitute into Eq. (29), the limit load is estimated. By doing this, the displacement values of 0.4226 m and 1.5774 m are obtained. In addition, the limit loads are about $\pm 148,102$ kN. Next; this structure is analyzed in seven ways, and the responses are displayed in Table 1. Figure 3 shows the load-displacement curve. It is demonstrated that the result of the authors' computer program is the same as the

reference [27]. In other words, the authors' answer is the same as the previous researchers' solution. This shows that the proposed method has good accuracy.

According to the obtained responses, the MEW and ZWI techniques are not able to analyze the truss. Other methods have more or less the same force-displacement diagram. However, the number of convergence points, the number of iterations, and their analysis time are different. Furthermore, the MKE and MDI methods have the same convergence points and the number of iterations. In fact, these strategies have behaved similarly in analyzing this truss. According to Figure 3, the structure enters the post-buckling region after the force value reaches 147,192 kN. In other words, this load is a snap-through point. The corresponding displacement of this force is 386.1 mm. After this point, the structure is unstable. Another limit point of the load occurred at the load of -147.428 kN and the deflection of 1609 mm. The number of convergences increments between snap-through points in MRF, MRE, MDI, MKE, and MRaKE procedures are 74, 70, 74, 74, and 72, correspondingly. There are two zero-load points in this truss. The top deflection corresponding to these points is equal to 1 and 2 meters. The top node is in the horizontal plane at the first state. The deflection of 2 m indicates that the structure is symmetric with its original shape and relative to the horizontal plane.

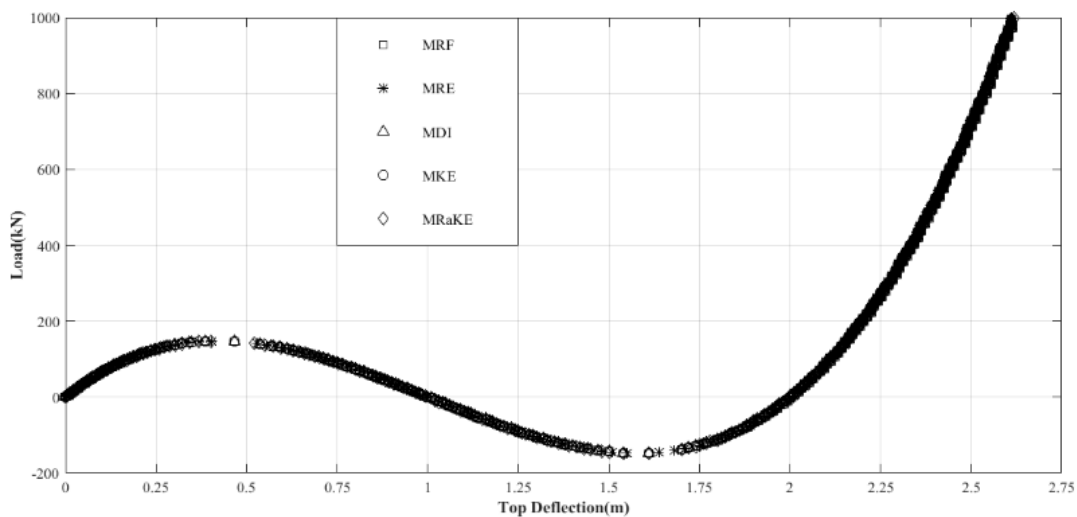


Figure 3: load-displacement curve for two members' truss

The analysis duration, the number of iterations, and the scores of the studied algorithms are shown in Table 2. The numbers in the two arcs indicate the rank of each process. Table 2 shows that based on S1, the MRF solution has the highest accuracy. The proposed MRaKE method is in the third rank. The S2 score demonstrates the superiority of the new scheme over the other techniques. In other words, the proposed method has the fastest convergence rate and the highest number of iterations in a short time. The MRF approach also has the slowest convergence rate. Therefore, this procedure is in the final rank. Based on the S3 rating, the suggested formula ranks fourth. MEW and ZWI could not reach the responses.

Table 2: The analysis results for two members' truss

| Technique | Number of convergence points | Number of iterations | analysis time (Second) | Ranking based on S1 & S1 Score | Ranking based on S2 & S2 Score | Ranking based on S3 & S3 Score |
|-----------|------------------------------|----------------------|------------------------|--------------------------------|--------------------------------|--------------------------------|
| MRF | 795 | 398 | 1.436 | 1.99749 (1) | 553.621 (5) | 0.00361 (1) |
| MRE | 4303 | 368 | 6.084 | 11.6929 (4) | 707.265 (2) | 0.01653 (5) |
| MDI | 1192 | 398 | 1.779 | 2.99497 (2) | 670.039 (3) | 0.00447 (2) |
| MKE | 1192 | 398 | 1.95 | 2.99497 (2) | 611.282 (4) | 0.0049 (3) |
| MEW | --- | --- | --- | --- | --- | --- |
| ZWI | --- | --- | --- | --- | --- | --- |
| MRaKE | 4060 | 377 | 5.491 | 10.7692 (3) | 739.392 (1) | 0.1456 |

4.2. The dome truss

In this part, the analysis of the dome truss in Figure 4 is performed. All the lower-level nodes are pinned supports. This truss has 25 nodes, 64 members, and 51 degrees of freedom. A concentrated force is applied to the tip node. The elasticity modulus and members' area are 205.947 GPa and 100 cm², respectively [17].

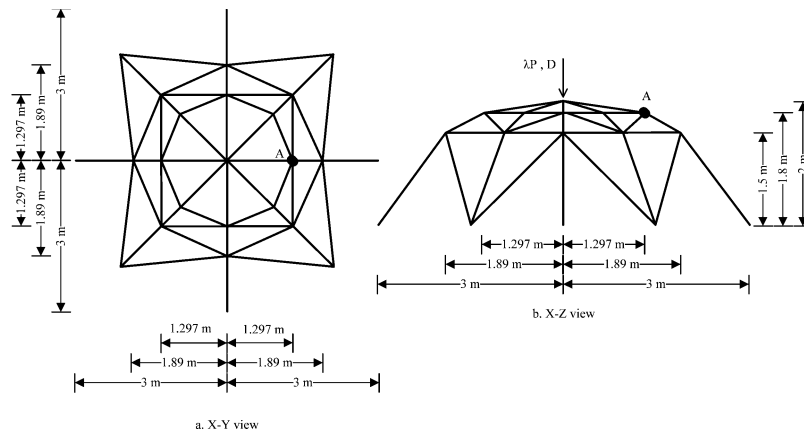


Figure 4: The geometry of the dome truss

Figure 5 shows the horizontal displacement of node A and the tip deflection curves against load P. All of the utilized methods can analyze the truss thoroughly. However, there are jumps between convergence points in MRF, MEW, and ZWI techniques. This jump was significant for the MEW method. As a result, this process is abandoned due to the inability to properly trace this structure. The MRF approach jumps are between load factors of 1.83454 and -1.77236 and for ZWI between 2.35339 and -2.29036. Hence, these two procedures will have the last two ranks. Based on Figure 5, this truss has load and displacement limit load points. The first snap-through of this structure occurs at the load of 5537.8 kN. The tip deflection at this point is 7.445 cm. This is the maximum force that the truss can sustain in a stable state. After that, the load returns, and its value will decrease. This reduction in the force continues until it reaches another limit load point. This occurs at the load of -4605.9 kN and the tip deflection of 29.71 cm. Then, the static path is placed on the second ascending branch. It should be noted that the displacement limit point of the

dome truss occurred at the load of -1381.6 kN. The horizontal displacement of node A at this point is 8.655 mm. In addition to this point, this structure has two zero-load configurations. At one of these points, the tip deflection is equal to 40 cm. In this case, the horizontal displacement A is zero. The deflection of 40 cm means that the tip node is in symmetry with the original shape relative to the level plate below the tip (level A).

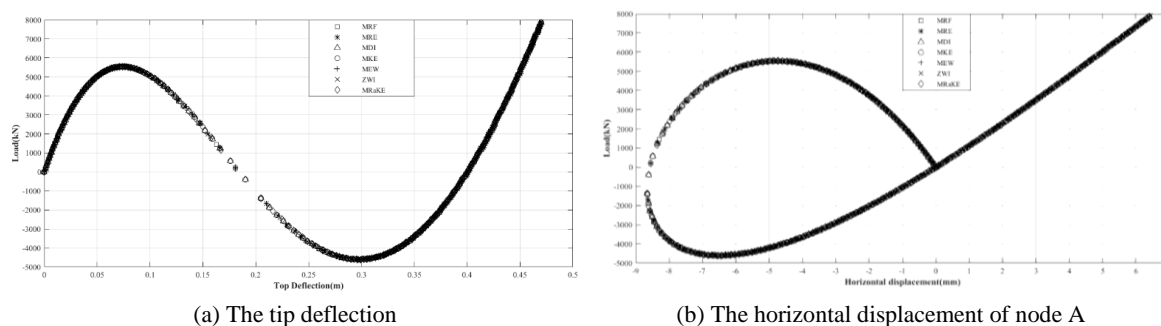


Figure 5: The load-displacement curve of the dome truss

Table 3 shows the results of analyzing this structure. Based on the indicator, the MRF algorithm ranks first. However, due to the jump event, this approach gained the fifth rank. The best schemes are MRE and MRaKE techniques for analyzing this truss.

Table 3: The analysis results for the dome truss

| Technique | Number of convergence points | Number of iterations | analysis time (Second) | Ranking based on S1 & S1 Score | Ranking based on S2 & S2 Score | Ranking based on S3 & S3 Score |
|-----------|------------------------------|----------------------|------------------------|--------------------------------|--------------------------------|--------------------------------|
| MRF | 13409 | 78 | 18.922 | 171.91 (5) | 708.646 (5) | 0.24259 (5) |
| MRE | 34894 | 163 | 50.085 | 214.074 (1) | 696.696 (6) | 0.30727 (2) |
| MDI | 55279 | 249 | 78.609 | 222.004 (3) | 703.215 (3) | 0.3157 (4) |
| MKE | 55305 | 249 | 77.828 | 222.108 (4) | 710.605 (1) | 0.31256 (3) |
| MEW | --- | --- | --- | --- | --- | --- |
| ZWI | 63317 | 258 | 89.887 | 245.415 (6) | 704.407 (4) | 0.3484 (6) |
| MRaKE | 40644 | 189 | 57.61 | 215.048 (2) | 705.503 (2) | 0.30481 (1) |

4.3. The Schwedler truss

Here, the structure in Figure 6 is analyzed. This truss has 240 members, 97 nodes, and 219 degrees of freedom. The Young's module and cross-section of each member are 21 GPa and 4.5 cm², correspondingly [18]. The lowest-level truss nodes are simply supported.

Figure 7 shows the diagram of load-displacement for tip node 1 and node 2. The result of the authors' method is the same as the references [18]. All approaches give more or less the same curve. This must be emphasized that the MRF solution has a local jump. This jump occurs in the post-buckling part. The jump is from load 78.1266 to -64.8198 N. This jump occurs near the snap-back point. Furthermore, the forces jump of MRE, MDI, MKE, MEW, ZWI, and MRaKE procedures are 39.5292, 76.5768, 76.5768, 124.7826, 81.5652 and 39.3336 N, respectively. These results indicate that the proposed technique and MRE

solution have the least jumps. Other schemes have jumped two to three times more than the authors' method. In other words, the MRE and MRaKE processes are the most accurate for analyzing this truss. According to the obtained results, the MKE and MDI methods have the same convergence points and the number of iterations. To explain it more clearly, these two approaches analyze this truss similarly. As it is demonstrated in Figure 7, the load limit point was obtained at a force of 453.2484 N and a displacement of 107.1 mm. In addition, the diagram of node 2 has a displacement limit point. This point occurs when the tip deflection reaches 276.8 mm. In this case, the horizontal displacement of node 2 is 4.336 mm. Although the MRaKE solution has fewer convergence points than the MDI, MKE, and ZWI procedures, its accuracy is good. In fact, the distance between the converged points in MDI, MKE, and ZWI solutions is very small. In the suggested method, the number of convergence points increases adjacent to the limit points. However, if the structural static path on the branch is stable, the number of these points will be less than the three solutions MDI, MKE, and ZWI.

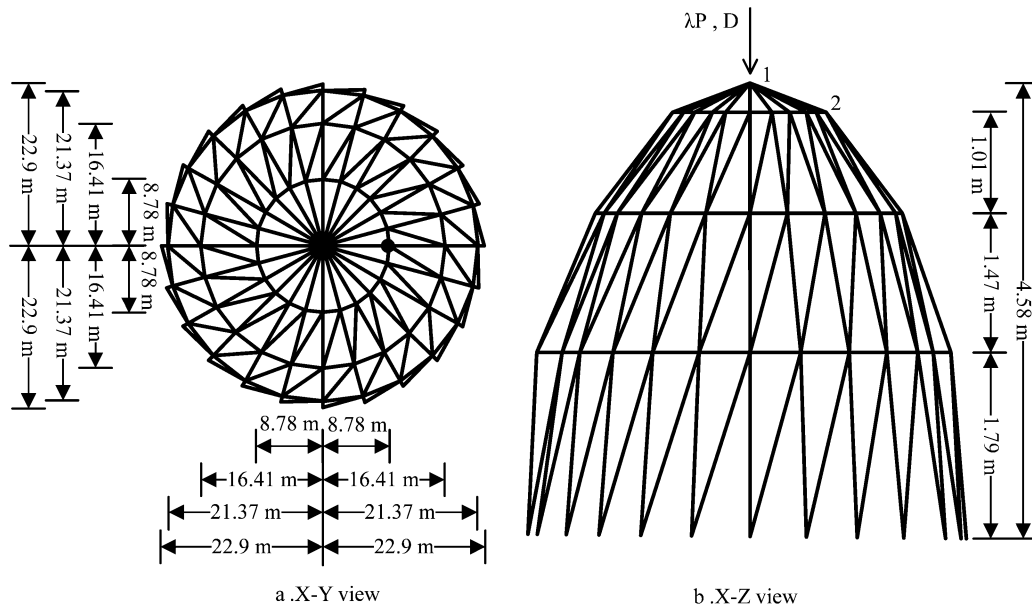


Figure 6: The Schwedler truss geometry

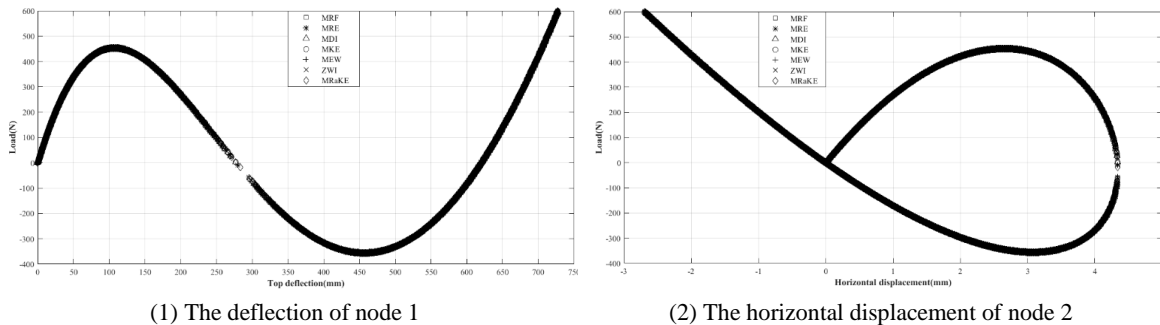


Figure 7: The load-displacement curve of the Schwedler truss

The analysis results of this study are listed in Table 4. This table shows that the structural analysis time of the proposed process is 40% less than that of the MDI and MKE schemes. This short time with proper accuracy is one of the features of the authors' technique. The large number of convergence points of MDI and MKE schemes increases the analysis duration. According to Table 4, the MRE and MRaKE methods are the best ways to analyze the dome truss. As mentioned before, this article aims to reduce the duration of structural analysis. Table 4 shows that for this relatively large truss, the time to reach the exact answer is less compared to other methods.

Table 4: The analysis results for the Schwedler truss

| Technique | Number of convergence points | Number of iterations | analysis time (Second) | Ranking based on S1 & S1 Score | Ranking based on S2 & S2 Score | Ranking based on S3 & S3 Score |
|-----------|------------------------------|----------------------|------------------------|--------------------------------|--------------------------------|--------------------------------|
| MRF | 86121 | 259 | 159.479 | 332.514 (5) | 540.015 (6) | 0.61575 (7) |
| MRE | 510173 | 1222 | 948.045 | 417.49 (4) | 538.132 (2) | 0.77581 (2) |
| MDI | 902750 | 2187 | 1724.93 | 412.78 (3) | 523.356 (3) | 0.78872 (3) |
| MKE | 902728 | 2187 | 1843.35 | 412.77 (3) | 489.722 (5) | 0.84287 (5) |
| MEW | 462775 | 1138 | 924.629 | 406.656 (1) | 500.498 (4) | 0.8125 (4) |
| ZWI | 881936 | 2198 | 1621.9 | 401.245 (6) | 543.766 (7) | 0.7379 (6) |
| MRaKE | 631691 | 1533 | 1043.67 | 412.062 (2) | 605.258 (1) | 0.68081 |

4.4. The star truss

Figure 8 shows a star truss. This structure is analyzed when carrying the symmetrical loading [13]. This space truss has 13 nodes and 21 degrees of freedom. Nodes 8 to 13 are pinned support. The module of elasticity and cross-section of the members are 303 GPa and 3.17 mm², respectively. The load applied to node 1 is twice the force applied to nodes 2, 3, 4, 5, 6, and 7. The amount of this load is 25 N.

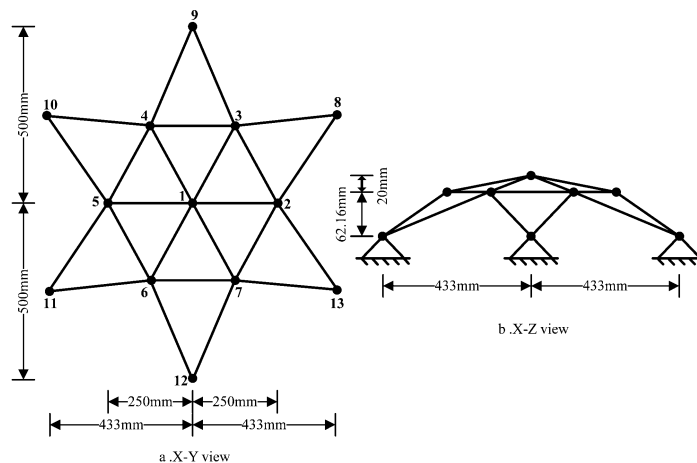


Figure 8: The star truss geometry

Figure 9 plots the static path of the truss tip (node 1) and node 2. The vertical axis of these diagrams shows the load value at the tip node. There are two load limit points for the

vertical displacement of node 1. These loads are 398.3785 and -225.418 N. The related displacements are 7.821 and 29.1 mm, correspondingly. The snap-through points for the deflection of node 2 occur at 376.308 and -206.205 N. The vertical displacements of node 2 are 0.8552 and -1.689 mm at these points, respectively. It should be noted that the MRF, MKE, MEW, and ZWI methods have significant jumps in the static path diagram. Because of this, these procedures are not able to trace the truss static path. Other processes have the appropriate answers. These ways trace all the limit points. However, the number of convergence points varies. Actually, the MDI and MRaKE methods trace the structural static path with more increments. For example, the numbers of convergence points for finding the limit points in the MRE, MDI, and MRaKE techniques are 180, 363, and 204, respectively.

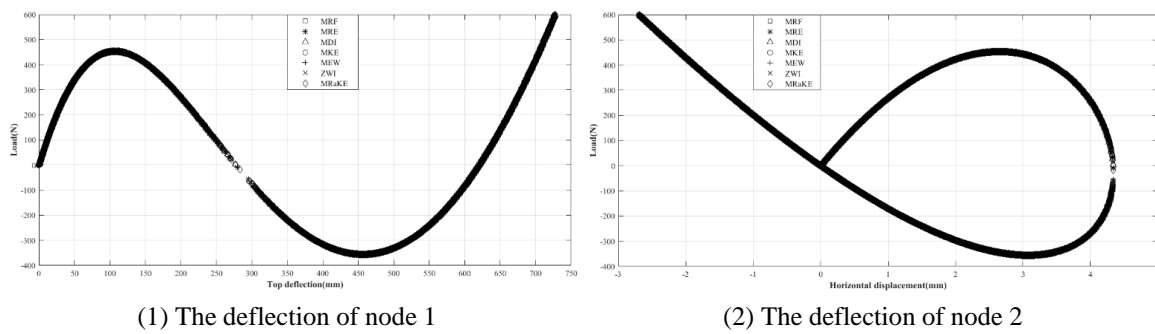


Figure 9: The load-displacement curve of the star truss

The results are listed in Table 5. Based on the number of convergent points on the structural static path, the analysis time, and the number of iterations, the MRaKE process falls between the MRE and MDI procedures. Criteria S2 and S3 indicate the authors' formulation suitability. In other words, in terms of truss analysis time, the MRaKE method is faster than the other schemes. Table 5 shows that the analysis of this structure with MRE and MRaKE algorithms leads to better results.

Table 5: The analysis results for the star truss

| Technique | Number of convergence points | Number of iterations | analysis time (Second) | Ranking based on S1 & S1 Score | Ranking based on S2 & S2 Score | Ranking based on S3 & S3 Score |
|-----------|------------------------------|----------------------|------------------------|--------------------------------|--------------------------------|--------------------------------|
| MRF | ---- | ---- | ---- | ---- | ---- | ---- |
| MRE | 170136 | 1063 | 244.156 | 160.053 (1) | 696.833 (2) | 0.22969 (2) |
| MDI | 246059 | 1490 | 373.137 | 165.14 (2) | 659.433 (3) | 0.25043 (3) |
| MKE | ---- | ---- | ---- | ---- | ---- | ---- |
| MEW | ---- | ---- | ---- | ---- | ---- | ---- |
| ZWI | ---- | ---- | ---- | ---- | ---- | ---- |
| MRaKE | 206373 | 1240 | 261.144 | 166.43 (3) | 790.265 (1) | 0.2106 |

4.5 The cylindrical roof

In another part of this research, the ability of the authors' method to solve shell structures is examined. To reach a proper conclusion, three different shells are analyzed. First, the

cylindrical roof of Figure 10 is analyzed. The two edges in the X direction are free, and the other two edges are simply supported. This structure is symmetric. For this reason, a quarter of the shell is analyzed. This roof is modeled by 100 shell elements. The shell thickness is 6.35 mm. Moreover, the Poisson's ratio and the modulus of elasticity are 0.3 and 3.10275 GPa, correspondingly [30]. All nodes located in the directions of AB and AC have the same uniform load [18].

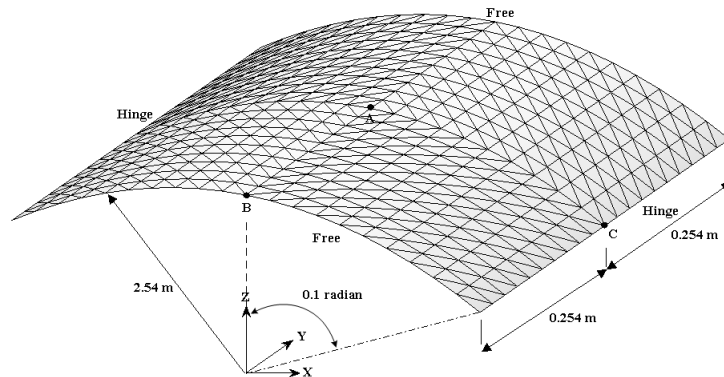
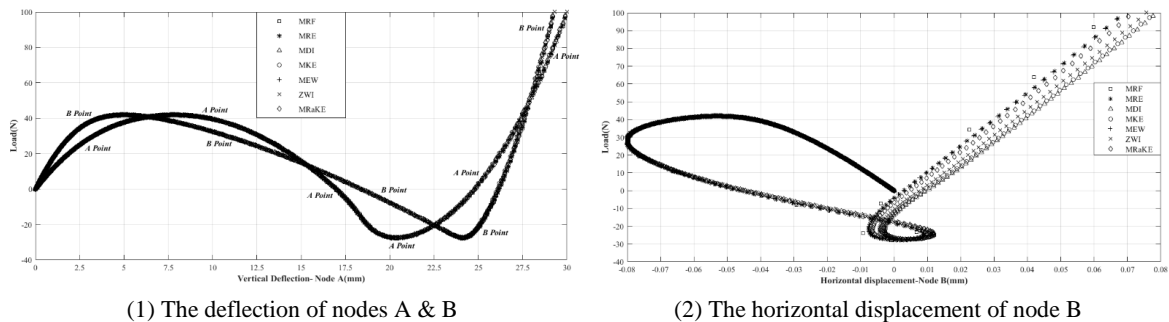


Figure 10: The cylindrical roof

Figure 11 shows the load-displacement diagrams of nodes A and B. The displacement of the limit point in the node B diagram increases the number of iterations required to trace the static path. This issue leads to an increase in the analysis time. This shell has 5 snap points. The first snap-through point occurred at the load of 41.9205 N. The deflection of points A and B and the horizontal displacement of B at this load were 7.825, 4.991, and 0.0528 mm, respectively. After this action, the structure enters the post-buckling part. The other snap-through occurred at a load of -27.395 N. The mentioned displacements are 20.333, 24.087, and 0.00507 mm, respectively. The three displacement limit points in the curve of node B are estimated to be 28.3682, -24.3011, and -26.5051 N, correspondingly. Table 6 shows the results of the analysis of this roof. The MRF method achieves very few convergence points. In other words, this approach has the least accuracy and ranks the last one. Nevertheless, this scheme traces the structural static path completely. Based on Table 6, the ZWI procedure and the proposed MRaKE technique are the best schemes for analyzing the cylindrical roof.



(1) The deflection of nodes A & B

(2) The horizontal displacement of node B

Figure 11: The load-displacement curve of the star truss

Table 6: The analysis results for the cylindrical roof

| Technique | Number of convergence points | Number of iterations | analysis time (Second) | Ranking based on S1 & S1 Score | Ranking based on S2 & S2 Score | Ranking based on S3 & S3 Score |
|-----------|------------------------------|----------------------|------------------------|--------------------------------|--------------------------------|--------------------------------|
| MRF | 101126 | 77 | 637.963 | 1313.32 (7) | 158.514 (7) | 8.28523 (7) |
| MRE | 1183477 | 322 | 7334.57 | 3675.39 (4) | 161.356 (6) | 22.7782 (6) |
| MDI | 1728985 | 458 | 9968.5 | 3775.08 (6) | 173.445 (3) | 21.7653 (5) |
| MKE | 1683197 | 450 | 9498.47 | 3740.44 (5) | 177.207 (1) | 21.1077 (4) |
| MEW | 1087139 | 321 | 6418.63 | 3386.73 (2) | 169.372 (5) | 19.9957 (2) |
| ZWI | 1458540 | 453 | 8591.51 | 3219.74 (1) | 169.765 (4) | 18.9658 (1) |
| MRaKE | 1316360 | 371 | 7459.2 | 3548.14 (3) | 176.475 (2) | 20.1057 |

4.6. The two-bay cylindrical shell

Figure 12 demonstrates the structural static path for the shell. Figure 12 demonstrates the static path for this structure. Due to symmetry, a quarter of this shell is modeled with 300 elements. The elasticity module, thickness, and Poisson’s ratio are 20 GPa, 3 cm, and 0.3, correspondingly [16, 18].

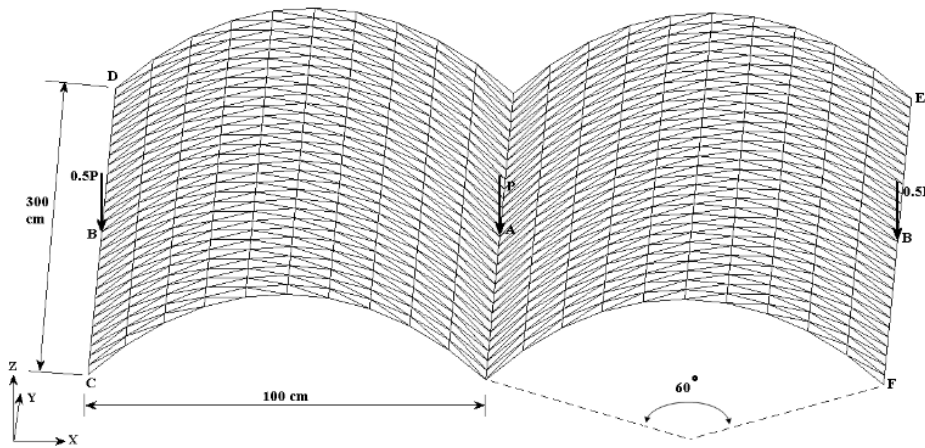


Figure 12: The two-bay cylindrical shell

Figure 13 shows the load-displacement curve of nodes A and B. According to Figure 13, the snap-back point starts at 57.6984 kN. At this load, the horizontal displacement of node B, and the deflections of A and B are 3.9725, 61.95, and 34.081 mm, respectively. Then, the snap-through point is formed at the force of 70.4889 kN. The aforementioned displacements for this point are 2.765, 116.484, and 50.548 mm, correspondingly. According to Figure 13, the structural static path has another snap-through point. The magnitude of the load and the deflection of nodes A and B are 50.6229 kN, 220.368 mm, and 86.466 mm, respectively. The figure shows that after the second limit point, the answers of the methods for estimating the horizontal displacements of node B are separated from each other. Furthermore, Both methods MDI and MKE trace the same curve. Moreover, both MEW and MRE strategies behave similarly. The closest load-displacement diagram to the reference [18] is the MRaKE scheme.

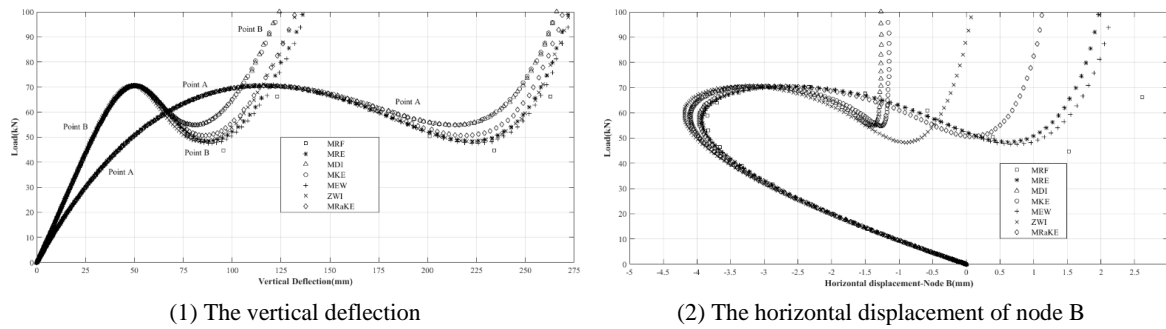


Figure 13: The equilibrium path of the two-bay cylindrical shell

Table 7 shows all outputs for this structure. According to the answers, the number of convergence points of the MRF process is much less than the other algorithms. According to the number of convergence points, the time to reach the answer of the proposed method was less compared to other methods. This is the goal of the writers in this article. The significant jumps of this procedure are shown in Figure 13. Therefore, this technique cannot trace this shell equilibrium path. Based on reference [18], the authors' method obtains more appropriate answers, and it has the first rank. The first and final steps of structural shape are shown in Figure 14.

Table 7: The analysis results for the two-bay cylindrical shell

| Technique | Number of convergence points | Number of iterations | analysis time (Second) | Ranking based on S1 & S1 Score | Ranking based on S2 & S2 Score | Ranking based on S3 & S3 Score |
|-----------|------------------------------|----------------------|------------------------|--------------------------------|--------------------------------|--------------------------------|
| MRF | ---- | ---- | ---- | ---- | ---- | ---- |
| MRE | 786277 | 133 | 6718.37 | 5911.86 (6) | 117.034 (4) | 50.5141 (4) |
| MDI | 1064745 | 183 | 9499.71 | 5818.28 (4) | 112.082 (5) | 51.911 (6) |
| MKE | 1062006 | 181 | 8742.38 | 5867.44 (5) | 121.478 (2) | 48.3004 (3) |
| MEW | 719557 | 133 | 6808.75 | 5410.2 (3) | 105.681 (6) | 51.1936 (5) |
| ZWI | 973924 | 182 | 8053.97 | 5351.23 (2) | 120.925 (3) | 44.2526 (2) |
| MRaKE | 897471 | 152 | 7413.08 | 5904.41 (1) | 121.066 (1) | 48.7703 (1) |

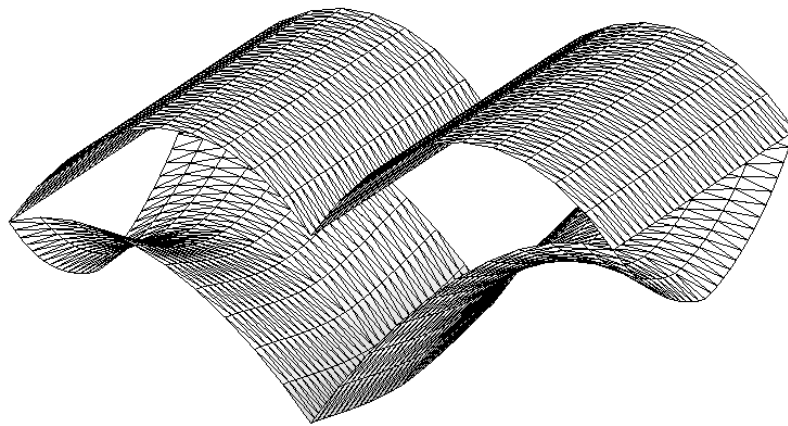


Figure 14: The first and final shape of the two-bay cylindrical shell

4.7. The shallow spherical cap

Figure 15 shows the geometry of this shell. Due to the symmetry in geometry and loading, a quarter of the shell can be modeled. The analysis is performed by utilizing 200 shell elements. All four corner nodes are located on the pinned support. Thickness, the modulus of elasticity, and Poisson's ratio are 99.45 mm, 68.944 GPa, and 0.3 mm, correspondingly. The force is applied at the crest cap [18].

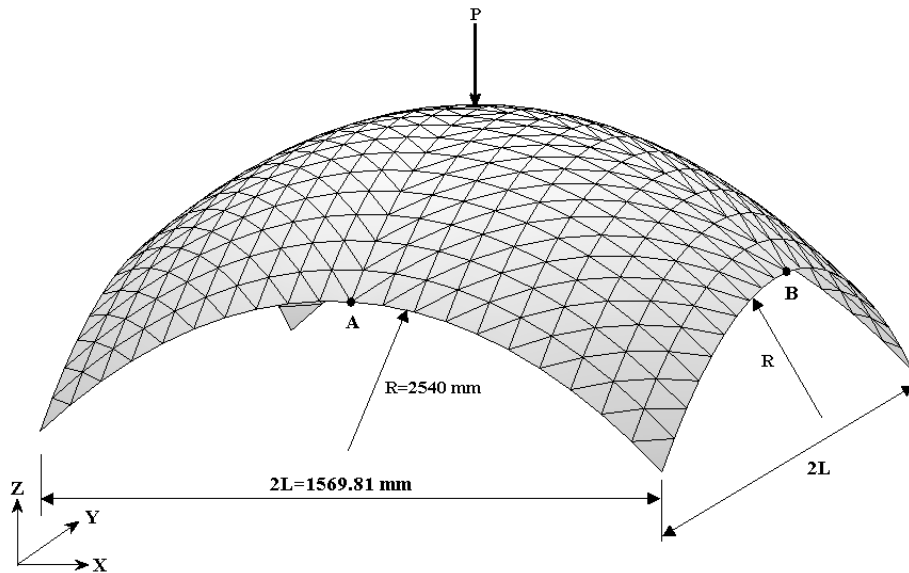
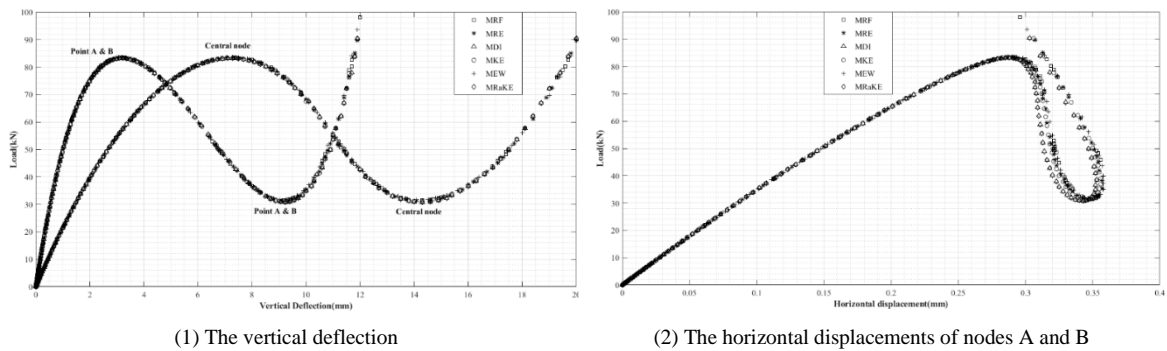


Figure 15: The shallow spherical cap geometry

In Figure 16, the static paths for the tip nodes, A and B, are plotted. For this shell, the first limit point occurs at 82,593 kN. Then, the displacement increases and the load decreases. This continues until the next limit point is reached. The related force for this point is equal to 31.2597 kN. Based on Figure 16, this structure has a displacement limit point. This is associated with the load 39.3372 kN. It should be noted that the snap-back region is after the second limit point. Figure 17 shows the initial and deformed shape of this spherical cap.



(1) The vertical deflection

(2) The horizontal displacements of nodes A and B

Figure 16: The load-displacement curves of the shallow spherical cap

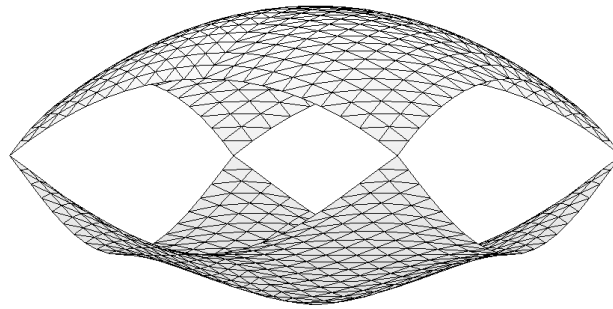


Figure 17: The first and final shape of the shallow spherical cap

The scores and rankings for the schemes are tabulated in Table 8. According to this, ZWI cannot analyze this shell. Therefore, no result is available for this technique. Furthermore, the number of converged points for the MRF solution is very small. Subsequently, the accuracy of this process is not appropriate. Thus, this scheme does not have any rankings. Both MDI and MKE methods have the same number of iterations and convergent points. In this example, the MEW algorithm has the highest accuracy. Based on all three criteria, the authors' scheme is third. Table 8 shows that the MRE process is the efficient strategy after MEW for solving this shell.

Table 8: The analysis results for the shallow spherical cap

| Technique | Number of convergence points | Number of iterations | analysis time (Second) | Ranking based on S1 & S1 Score | Ranking based on S2 & S2 Score | Ranking based on S3 & S3 Score |
|-----------|------------------------------|----------------------|------------------------|--------------------------------|--------------------------------|--------------------------------|
| MRF | 56426 | 25 | 352.327 | ---- | ---- | ---- |
| MRE | 395827 | 200 | 2588.88 | 1979.14 (2) | 152.895 (4) | 12.9444 (2) |
| MDI | 257759 | 97 | 1703.77 | 2657.31 (4) | 151.287 (5) | 17.5647 (5) |
| MKE | 257759 | 97 | 1543.9 | 2657.31 (4) | 166.953 (2) | 15.9165 (4) |
| MEW | 456732 | 272 | 2721.77 | 1679.16 (1) | 167.807 (1) | 10.0065 (1) |
| ZWI | ---- | ---- | ---- | ---- | ---- | ---- |
| MRaKE | 277583 | 120 | 1678 | 2313.19 (3) | 165.425 (3) | 13.9833 |

5. THE RANKS OF METHODS

The rank of each algorithm is estimated based on the number of convergence increments, the number of iterations, and the analysis time. To perform the comparative studies, the score of each process is obtained from Eq. (31). Here, the Q_{ij} symbol indicates the j -th ranks of method i -th. In other words, this factor indicates that process i has obtained j ranks several times. For example, the MRaKE procedure is four times the first technique, based on the S_2 and S_3 criteria. Therefore, Q_{i1} is equal to four for this scheme. Furthermore, the MRE process ranks third three times, based on the S_2 . Hence, Q_{i2} for this strategy is equal to three. The number of structures that the technique i could not analyze is denoted by Q_{i0} . For example, in one problem the MKE method is not able to reach the answer, for this reason, Q_{i0} is equal to one.

$$S_{ij} = 100 \times \sum_{j=1}^7 Q_{ij} \times (8-j) / 49 \tag{31}$$

It should be added that if a process is not able to reach the answer, Eq. (31) is not used for it. In addition, the number 49 is obtained when the method ranks first in all seven samples. As a result, the S_{ij} score for it will be 100. The final scores and ranks of all procedures are listed in Table 9 to Table 11. Based on these answers, the algorithms are ranked in Table 12. This table shows that the authors' scheme ranks first in all three criteria. The robustness feature of the proposed technique is the least time required to perform the analyses. This is shown by the difference between the first and second ranks in the S_2 and S_3 criteria. Table 12 shows that the MRF process is the worst way to trace the static path of structures.

Table 9: The rank of the techniques based on S_1

| Method | Q_{ij} | | | | | | | | S_i |
|--------|----------|-----|-----|-----|-----|-----|-----|-----|--------|
| | j=0 | j=1 | j=2 | j=3 | j=4 | j=5 | j=6 | j=7 | |
| MRF | 3 | 1 | 0 | 0 | 0 | 2 | 0 | 1 | 28.571 |
| MRE | 0 | 2 | 1 | 0 | 3 | 0 | 1 | 0 | 69.388 |
| MDI | 0 | 0 | 2 | 2 | 2 | 0 | 1 | 0 | 65.306 |
| MKE | 1 | 0 | 1 | 1 | 2 | 2 | 0 | 0 | 51.02 |
| MEW | 3 | 2 | 1 | 1 | 0 | 0 | 0 | 0 | 51.02 |
| ZWI | 3 | 1 | 1 | 0 | 0 | 0 | 2 | 0 | 34.694 |
| MRaKE | 0 | 1 | 2 | 4 | 0 | 0 | 0 | 0 | 79.592 |

Table 10: The rank of the techniques based on criterion S_2

| Method | Q_{ij} | | | | | | | | S_i |
|--------|----------|-----|-----|-----|-----|-----|-----|-----|--------|
| | j=0 | j=1 | j=2 | j=3 | j=4 | j=5 | j=6 | j=7 | |
| MRF | 3 | 0 | 0 | 0 | 0 | 2 | 1 | 1 | 18.367 |
| MRE | 0 | 0 | 3 | 0 | 2 | 0 | 2 | 0 | 61.224 |
| MDI | 0 | 0 | 0 | 5 | 0 | 2 | 0 | 0 | 63.265 |
| MKE | 1 | 2 | 2 | 0 | 1 | 1 | 0 | 0 | 67.347 |
| MEW | 3 | 1 | 0 | 0 | 1 | 1 | 1 | 0 | 32.653 |
| ZWI | 3 | 0 | 0 | 1 | 2 | 0 | 0 | 1 | 28.571 |
| MRaKE | 0 | 4 | 2 | 1 | 0 | 0 | 0 | 0 | 91.837 |

Table 11: The rank of the techniques based on criterion S_3

| Method | Q_{ij} | | | | | | | | S_i |
|--------|----------|-----|-----|-----|-----|-----|-----|-----|--------|
| | j=0 | j=1 | j=2 | j=3 | j=4 | j=5 | j=6 | j=7 | |
| MRF | 3 | 1 | 0 | 0 | 0 | 1 | 0 | 2 | 24.49 |
| MRE | 0 | 0 | 4 | 0 | 1 | 1 | 1 | 0 | 67.347 |
| MDI | 0 | 0 | 1 | 2 | 1 | 2 | 1 | 0 | 57.143 |
| MKE | 1 | 0 | 0 | 3 | 2 | 1 | 0 | 0 | 53.061 |
| MEW | 3 | 1 | 1 | 0 | 1 | 1 | 0 | 0 | 40.816 |
| ZWI | 3 | 1 | 1 | 0 | 0 | 0 | 2 | 0 | 34.694 |
| MRaKE | 0 | 4 | 0 | 2 | 1 | 0 | 0 | 0 | 85.714 |

Table 12: Final ranking of the methods

| Criteria | Grade | | | | | | |
|----------|-------|-----|-----|-----------|-----|-----|------|
| | 1 | 2 | 3 | 4 | 5 | 6 | 7 |
| S1 | MRaKE | MRE | MDI | MKE & MEW | ZWI | MRF | ---- |
| S2 | MRaKE | MKE | MDI | MRE | MEW | ZWI | MRF |
| S3 | MRaKE | MRE | MDI | MKE | MEW | ZWI | MRF |

6. CONCLUSIONS

According to the findings, one of the most prominent features of the authors' scheme is the high convergence rate with appropriate accuracy. In other words, the new process greatly reduces the analysis time compared to other methods; while its accuracy is not significantly lessened from the other ways. Applying the load factor in the proposed method is free from analyst choice, and it is unconditional. Essentially, the new procedure only utilizes dynamic relaxation parameters. It should be remembered that user intervention is required in arc-length algorithms. Moreover, the number of iterations and convergence points and the analysis time depend on the length of the arc. Besides, the low number of convergence increments reduces the analysis time. In other words, the proposed method was able to obtain each converged point in less time. Also, the authors' approach required less time for the calculations of one iteration.

DECLARATIONS

It is confirmed that the Availability of data and material, Funding, Authors' contributions, Acknowledgments, and all the subheadings of these and also the relevant information under each have been declared in this paper. Moreover, there is no conflict of interest.

THE DATA AVAILABILITY

By giving the paper reference, all the data that support the findings of this study are available to the researchers.

REFERENCES

1. Topping B. H. V., Iványi P. *Computer-Aided Design of Cable Membrane Structures*. Scotland: Saxe-Coburg Publications; 2008. 39–84.
2. Alamatian J. A new formulation for fictitious mass of the Dynamic Relaxation method with kinetic damping. *Comput Struct*. 2012; **90–91**:42-54.
3. Namadchi A. H., Alamatian J. Explicit dynamic analysis using dynamic relaxation method. *Comput Struct*. 2016; **175**:91-99.
4. Jung S., Kim T-Y., Yoo W-S. Adaptive step-size control for dynamic relaxation using continuous kinetic damping. *Math Probl Eng*. 2018; 1–9.

5. Rezaiee-Pajand M., Mohammadi-Khatami M. A fast and accurate dynamic relaxation scheme. *Front Struct Civ Eng*. 2019; **13**:176-89.
6. Hüttner M., Máca J., Fajman P. The efficiency of dynamic relaxation methods in static analysis of cable structures. *Adv Eng Softw*. 2015; **89**:28-35.
7. Rezaiee-Pajand M., Estiri H., Mohammadi-Khatami M. Creating better dynamic relaxation methods. *Eng Comput*. 2019; **36**:1483-521.
8. Barnes M., Topping B., Wakefield D. Aspects of form finding by dynamic relaxation. London, United Kingdom; 1977.
9. Barnes M. R. Form finding and analysis of tension structures by dynamic relaxation. *Int J Space Struct*. 1999; **14**:89-104.
10. Moncrieff E., Topping B. H. V. Computer methods for the generation of membrane cutting patterns. *Comput Struct*. 1990; **37**:441-50.
11. Topping B., Khan A. Parallel computation schemes for dynamic relaxation. *Eng Comput*. 1994; **11**:513-48.
12. Lee K. S., Han S. E., Park T. A simple explicit arc-length method using the dynamic relaxation method with kinetic damping. *Comput Struct*. 2011; **89**:216-33.
13. Rezaiee-Pajand M., Alamatian J. Automatic DR structural analysis of snap-through and snap-back using optimized load increments. *J Struct Eng*. 2011; **137**:109-16.
14. Alamatian J. Displacement-based methods for calculating the buckling load and tracing the post-buckling regions with dynamic relaxation method. *Comput Struct*. 2013; **114–115**:84-97.
15. Lee K-S., Han S-E., Hong J-W. Post-buckling analysis of space frames using concept of hybrid arc-length methods. *Int J Non-Linear Mech*. 2014; **58**:76-88.
16. Rezaiee-Pajand M., Estiri H. Computing the structural buckling limit load by using dynamic relaxation method. *Int J Non-Linear Mech*. 2016; **81**:245-60.
17. Rezaiee-Pajand M., Estiri H. Mixing dynamic relaxation method with load factor and displacement increments. *Comput Struct*. 2016; **168**:78-91.
18. Rezaiee-Pajand M., Estiri H. Finding equilibrium paths by minimizing external work in dynamic relaxation method. *Appl Math Model*. 2016; **40**:10300-22.
19. Rezaiee-Pajand M., Estiri H. Finding buckling points for nonlinear structures by dynamic relaxation scheme. *Front Struct Civ Eng*. 2020; **14**:23-61.
20. Golmakani M. E., Zeighami V. Nonlinear thermo-elastic bending of functionally graded carbon nanotube-reinforced composite plates resting on elastic foundations by dynamic relaxation method. *Mech Adv Mater Struct*. 2018; **25**:868-80.
21. Golmakani M. E., Kadkhodayan M. An investigation into the thermoelastic analysis of circular and annular functionally graded material plates. *Mech Adv Mater Struct*. 2014; **21**:1-13.
22. Iványi P. CUDA accelerated implementation of parallel dynamic relaxation. *Adv Eng Softw*. 2018; **125**:200-8.
23. Ni T., Zaccariotto M., Zhu Q-Z., Galvanetto U. Coupling of FEM and ordinary state-based peridynamics for brittle failure analysis in 3D. *Mech Adv Mater Struct*. 2021; **28**:875-90.

24. Underwood P. Dynamic relaxation (in structural transient analysis). *Comput Methods Transient Anal.* 1983; 245-65.
25. Zhang L. G., Yu T. X. Modified adaptive dynamic relaxation method and its application to elastic-plastic bending and wrinkling of circular plates. *Comput Struct.* 1989; **33**:609-14.
26. Rezaiee-Pajand M., Alamatian J. The dynamic relaxation method using new formulation for fictitious mass and damping. *Struct Eng Mech.* 2010; **34**:109-33.
27. Greco M., Menin R., Ferreira I., Barros F. Comparison between two geometrical nonlinear methods for truss analyses. *Struct Eng Mech.* 2012; **41**:735-50.
28. Greco M., Vicente C. E. R. Analytical solutions for geometrically nonlinear trusses. *Rem Rev Escola Minas.* 2009; **62**:205-14.
29. Felippa C. A. *Nonlinear Finite Element Methods (ASEN 5017)*. University of Colorado, Boulder, Colorado, USA; 2001.
30. Boutagouga D., Gouasmia A., Djeghaba K. Geometrically nonlinear analysis of thin shell by a quadrilateral finite element with in-plane rotational degrees of freedom. *Eur J Comput Mech.* 2010; **19**:707-24.